Original article
DOI: https://doi.org/10.18721/JPM.19205

THE INFLUENCE OF A SILICA TRENCH PROFILE ON THE PHOTOSENSITIVITY OF A CMOS-COMPATIBLE AVALANCHE PHOTODIODE IN THE VISIBLE RANGE

D. I. Dolzhenko✉, *E. D. Letkiman*

Peter the Great St. Petersburg Polytechnic University, St. Petersburg, Russia

✉ ddi.dev.94@gmail.com

Abstract. This work has involved the simulation of technological operations of manufacturing a silicon (Si) avalanche photodiode and calculating its output characteristics. As a result, the values of its multiplication factor (from 49.5 to 62.3) and spectral sensitivity (from 15.8 to 19.6 A/W) depending on the shallow trench insulation defect type are presented for a Si avalanche photodiode. It has been shown that the technological defects causing narrowing of the width of the trench towards its bottom have the greatest impact on these parameters. As a result, the multiplication factor decreases by up to 18%. The dependence of the photodiode gain on the trench's wall inclination angle was established to be described well by a linear function. It was also demonstrated that the trench narrowing led to an increase in the lateral component of the electric field strength near the groove, which reduced the breakdown voltage, but did not lead to an increase in multiplication.

Keywords: avalanche photodiode, multiplication factor, spectral sensitivity, technological defects, STI, TCAD

Citation: Dolzhenko D. I., Letkiman E. D., The influence of a silica trench profile on the photosensitivity of a CMOS-compatible APD in the visible range, St. Petersburg State Polytechnical University Journal. Physics and Mathematics. 19 (2) (2026) 57–67. DOI: https://doi.org/10.18721/JPM.

This is an open access article under the CC BY-NC 4.0 license (https://creativecommons.org/licenses/by-nc/4.0/)

Научная статья
УДК 621.383.523
DOI: https://doi.org/10.18721/JPM.19205

ВЛИЯНИЕ ПРОФИЛЯ ТРАНШЕИ ИЗ ДИОКСИДА КРЕМНИЯ НА ФОТОЧУВСТВИТЕЛЬНОСТЬ КМОП-СОВМЕСТИМОГО ЛАВИННОГО ФОТОДИОДА ВИДИМОГО ДИАПАЗОНА

Д. И. Долженко✉, *Е. Д. Леткиман*

Санкт-Петербургский политехнический университет Петра Великого,
Санкт-Петербург, Россия

✉ ddi.dev.94@gmail.com

Аннотация. В работе проведено моделирование технологических операций изготовления кремниевого лавинного фотодиода и расчет его выходных характеристик. В результате представлены значения его коэффициента умножения (62,3 – 49,5) и спектральной чувствительности (19,6 – 15,8 А/Вт) в зависимости от типа дефекта траншеи из диоксида кремния. Показано, что наибольшим образом на данные параметры влияют технологические дефекты, приводящие к сужению профиля траншеи (узкой щели) по направлению к ее дну, что приводит к снижению коэффициента умножения вплоть до 18%. Установлено, что зависимость усиления фотодиода от угла наклона стенки

© Dolzhenko D. I., Letkiman E. D., 2026. Published by Peter the Great St. Petersburg Polytechnic University.

траншеи хорошо описывается линейной функцией. Показано, что сужение траншеи вызывает увеличение латеральной компоненты напряженности электрического поля вблизи этой траншеи, что снижает значение пробивного напряжения и не увеличивает коэффициент умножения исследуемого фотодиода.

Ключевые слова: лавинный фотодиод, коэффициент умножения, спектральная чувствительность, технологические дефекты, STI, TCAD

Ссылка для цитирования: Долженко Д. И., Леткиман Е. Д. Влияние профиля траншеи из диоксида кремния на фоточувствительность КМОП-совместимого лавинного фотодиода видимого диапазона // Научно-технические ведомости СПбГПУ. Физико-математические науки. 2026. Т. 2 № .19. С. 57–67. DOI: https://doi.org/10.18721/JPM.19205

Статья открытого доступа, распространяемая по лицензии CC BY-NC 4.0 (https://creativecommons.org/licenses/by-nc/4.0/)

Introduction

CMOS-compatible avalanche photodiodes (APDs) are widely used in precision positioning devices, optical communication systems, and LIDAR (light detection and ranging) systems [1–4]. However, forming the cathode and anode on the silicon wafer surface poses several major challenges, the most significant of which are surface effects: non-uniform electric field distribution and surface leakage currents [5]. These factors can cause not only a sharp reduction in the avalanche multiplication factor across the entire spectral range but also premature surface breakdown of the wafer.

One promising solution is to form a narrow trench (a few micrometers wide) between the cathode and anode, filled with silica (SiO_2). This method is known as shallow trench isolation (STI) [6]. There are numerous methods for etching silicon, but as a rule, the stronger the anisotropy of the profile formed, the more complex the process and the higher the equipment requirements.

However, each approach has its drawbacks. This combination of factors does not always guarantee the desired field distribution and impact ionization paths, which affects the current values at a given supply voltage. In addition, different patterns of multiple reflection of light arise when the entire photosensitive area is illuminated (or when part of it is illuminated at an angle). In view of these unfavorable conditions, we can formulate the goal of our study:

to analyze how the profile of a trench filled with silica affects the current–voltage behavior of a CMOS-compatible avalanche photodiode.

Research methodology and description of the silicon avalanche photodiode structure

Calculations of the output characteristics and simulations of the fabrication process of the avalanche photodiode were carried out in the Sentaurus TCAD package. Despite the limitations of real photomask patterns, we treated the structure as axisymmetric in our simulations. This minimizes the edge effects, so that the resulting electric field distribution can be interpreted unambiguously. The donor (N_D) and acceptor (N_A) concentrations, as well as the change rates of these concentrations ΔN_D and ΔN_A near the p–n junction, were chosen so as to provide a sufficient slope of the current–voltage curve in the linear regime [7]. These conditions were chosen to observe the changes in the behavior of the current–voltage curve across all its regions.

The most common trench profiles and associated defects were used in the simulations (see Fig. 2). The corresponding fabrication technologies for these structures are listed in Table 1. Although the set of selected profiles is far from exhaustive, it provides insight into how the avalanche develops and how the field forms near the trench.

It was expected that some STI profile defects would not significantly affect the avalanche development or the multiplication factor. However, no preliminary selection is possible without simulation, since it is unrealistic to account for several simultaneous changes in the electric field distribution, ionization potential, and carrier mobility.

© Долженко Д. И., Леткиман Е. Д., 2026. Издатель: Санкт-Петербургский политехнический университет Петра Великого.

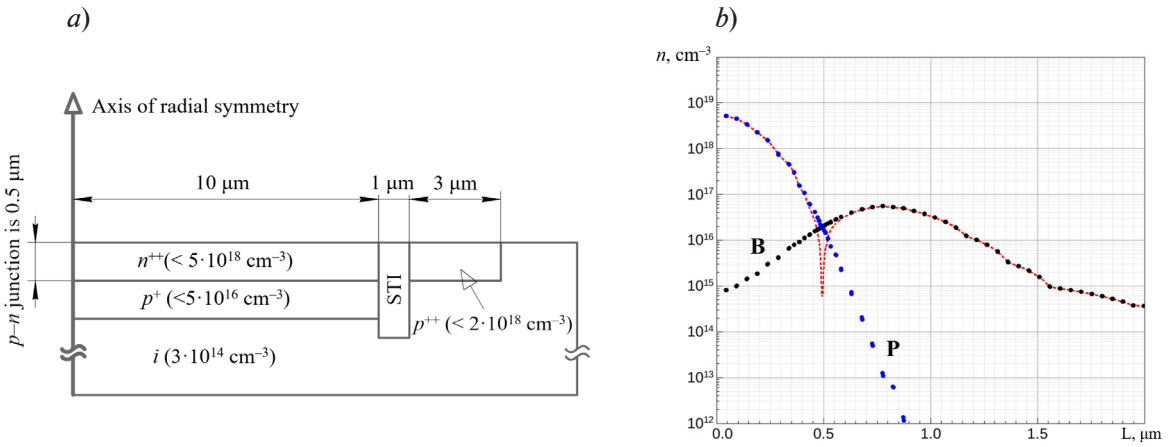


Fig. 1. Schematic of radial cross-section of the structure (*a*);
dopant (boron and phosphorus) concentration profiles versus depth in the photosensitive region (*b*)
The red curve shows the dopant concentration as an absolute value

A mesh convergence study is one of the first stages in simulations of a wide range of structures. We should note that two different mesh types are advisable for simulating fabrication processes and physics of semiconductor devices. An adaptive mesh is convenient for models of fabrication processes: its step a decreases as the change rate of the target quantity N_D with respect to the coordinate x increases, i.e., $1/a \sim dN_D/dx$. This mesh provides high accuracy and saves computational resources.

An adaptive mesh is unsuitable for simulating the physics of the resulting structure, because the cell size grows rapidly with depth, producing a significant error and often leading to a lack of solution convergence, especially in optics. Therefore, a mesh must be rebuilt before the simulation of the output characteristics, with a minimum step determined by a mesh convergence analysis.

Classical drift-diffusion equations and Poisson's equation for electron and hole concentrations, traditionally adopted in TCAD (Technology Computer-Aided Design) simulations of semiconductor structures, were used as the transport model. The standard set of physical models recommended for simulating silicon photodiodes [16] was used to describe generation and recombination mechanisms.

It is essential to discuss how avalanche parameters themselves are estimated for the avalanche photodiode. For the silicon structure, we estimated the breakdown electric field using the well-known ionization model [16, 17]. To this end, we calculated the ionization integrals for electrons and holes, which become equal to unity at silicon breakdown, using the following equations:

$$\int_0^W \alpha_n \exp\left(-\int_x^W (\alpha_n - \alpha_p)dx'\right)dx = 1, \quad \int_0^W \alpha_p \exp\left(-\int_x^W (\alpha_p - \alpha_n)dx'\right)dx = 1, \tag{1}$$

where α_n, α_p are the ionization coefficients for electrons and holes, respectively; W is the width of the space charge region; x, x' are the coordinates for the outer and inner integrals, respectively.

The ionization coefficients, in turn, can be estimated from the Van Overstraeten–De Man model [18] based on the Chynoweth equations [19], accurately describing ionization in the field range $(1–6)\cdot10^5$ V/cm near silicon breakdown:

$$\alpha_n(x) = \gamma\alpha_n \exp\left(-\frac{\gamma b_n}{E(x)}\right), \quad \alpha_p(x) = \gamma\alpha_p \exp\left(-\frac{\gamma b_p}{E(x)}\right), \tag{2}$$

where α_n, α_p, b_n, b_p are empirical model coefficients reflecting the ionization rate; $E(x)$ is the local electric field strength; γ is the phonon temperature correction.

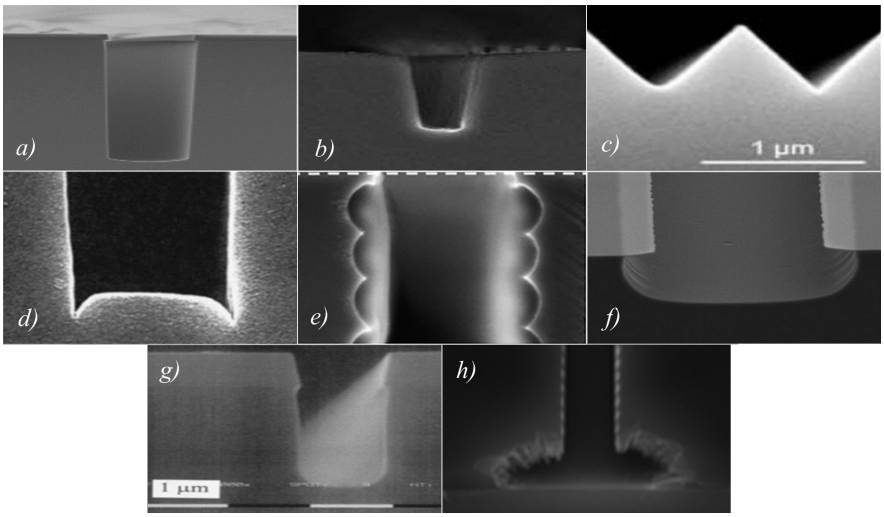


Fig. 2. Doping profiles with different defect types:
vertical, rectangular, anisotropic, with smooth sidewalls (*a*); trapezoidal, sidewall inclination angle ≥ 80° (most common) (*b*); V-shaped, with inclination angle < 80° (*c*); W-shaped, anisotropic, with microtrenching at the sidewall edges (*d*); scalloped (*e*); oval, hemispherical, isotropic (*f*); U-shaped, anisotropic (*g*); profile with undercut at the trench bottom (*h*). See Table 1 for the fabrication technologies

Table 1

Fabrication technologies for the doping profiles shown in Fig. 2

Position in Fig. 2	Technology	Source
a)	Dry etching (ICP-RIE)	[8]
b)	Dry etching	[9]
c)	KOH wet etching	[10]
d)	Reactive ion etching (RIE)	[11]
e)	Cyclic dry etching (BOSCH process)	[12]
f)	Isotropic SF_6 plasma etching	[13]
g)		[14]
h)	Reactive ion etching (RIE)	[15]

We used the following coefficient values:

$$\alpha_n = 7.03 \cdot 10^5 \text{ cm}^{-1},\ \alpha_p = (6.71\text{–}15.82) \cdot 10^5 \text{ cm}^{-1};$$

$$b_n = 1.231 \cdot 10^6 \text{ V/cm},\ b_p = (1.693\text{–}2.036) \cdot 10^6 \text{ V/cm}.$$

The choice of α_p and b_p within these intervals depended on the magnitude of $E(x)$.
The phonon temperature correction follows the expression

$$\gamma = \tanh\left(\frac{\hbar\omega}{2kT_0}\right) \Big/ \tanh\left(\frac{\hbar\omega}{2kT}\right), \tag{3}$$

where $\hbar\omega$ is the phonon energy ($\hbar\omega = 0.063$); T_0 is the temperature for which the empirical parameters are given.

Results and discussion

Simulation of such structures must begin with defining the geometric parameters of the trench profile whose shape is to be analyzed. The profile width typically does not exceed 1 μm [20, 21], while the STI depth is a variable parameter. Therefore, at the first stage, in addition to mesh convergence analysis, we assessed how the depth of the STI profile affects the current–voltage characteristic of the avalanche photodiode for a rectangular trench profile.

Both dependences in Fig. 3 show a significant drop in the multiplication factor M at a trench depth $L < 3$ μm. Despite a decrease in the supply voltage of about %10, M drops by about 72%. This is because when the depth of the STI, which acts as a guard ring, decreases, lateral avalanche processes become possible. The electric field distribution shifts increasingly toward the surface, and the lateral electric field near the surface (at small L) is several times stronger, since it is not confined by the silica trench.

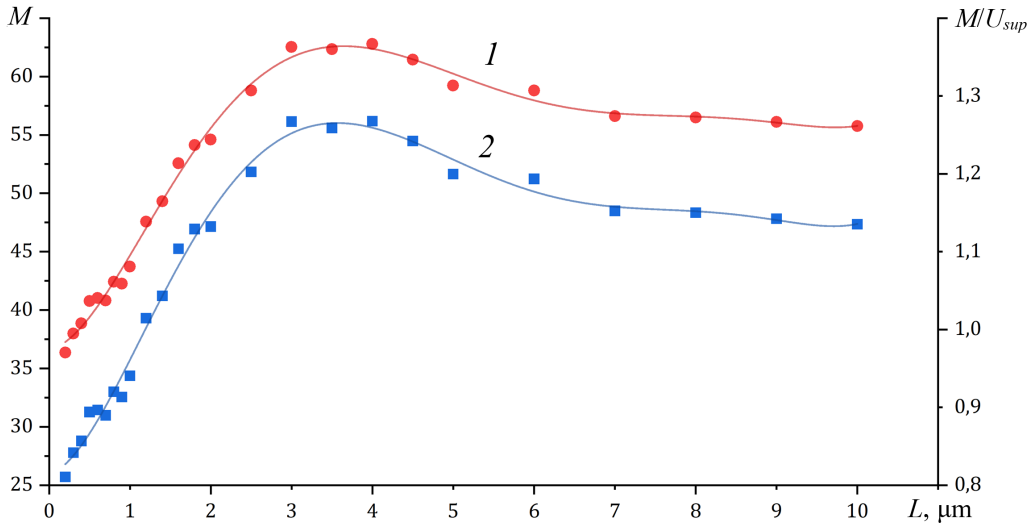


Fig. 3. Multiplication factor M (*1*) and its values normalized to the supply voltage, M/U_{sup} (*2*), as a function of STI profile depth
Supply voltage $U_{sup} = 0.98U_{br}$ (U_{br} is the breakdown voltage)

At $L > 4$ μm, the multiplication factor M begins to decrease gradually. As the depth increases, the field becomes more elongated, and the intensity at a wavelength of about 670 nm drops by about an order of magnitude already at a depth of 10 μm. The field strength decreases only slightly in the depth range below 10 μm, where most of the radiation is absorbed (here it is considerably closer to the STI region). At greater depths, the change rate of M gradually increases. Importantly, however, simulating greater depths is impractical, since it sharply reduces the number of available etching methods, requiring a high aspect ratio for the STI profile.

In the second stage, we turn to simulating profiles (trench width $W = 1$ μm, depth $L = 3$ μm) with different defect types. Note that fully isotropic etching cannot be implemented because of the unfavorable 3 : 1 aspect ratio. Fig. 4 shows the current–voltage curves for the photocurrent and the dark current. The breakdown voltage is predominantly influenced by the degree of narrowing toward the bottom of the STI trench, with a consequent increase in the contribution of the lateral field component to the avalanche process. Although the other defect types alter the field distribution near the edge of the photosensitive region, they have almost no effect on the breakdown voltage.

The resulting values of the multiplication factor and spectral sensitivity are listed in Table 2. Thus, defects associated with trench narrowing can reduce M by up to 18%.

For the W-shaped defect type, the values are almost identical to those of the idealized rectangular profile, because the formation of two depressions near the trench sidewalls can locally increase the trench depth to as much as 4 μm. According to the data in Fig. 3, the multiplication factor M remains essentially unchanged in the 3–4 μm range.

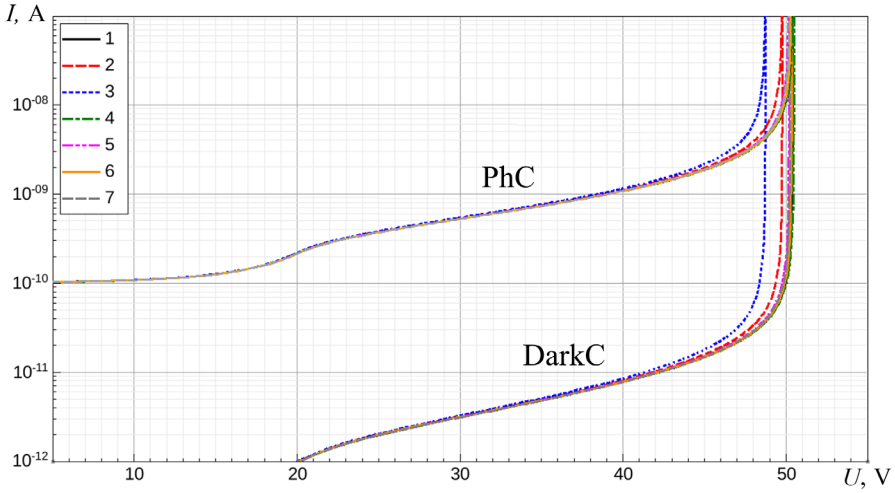


Fig. 4. Calculated I–V curves for the photocurrent (PhC) and dark current (DarkC) for different STI profile types and defects
The curve numbers correspond to the profile types in Table 2

Table 2

Key parameters of STI profile for different types of defects

Profile	S, A/W	M	U_{br}, V	M/U_{sup} (0.98 U_{br})
1. Rectangular	19.0	60.4	50.3	1.23
2. Trapezoidal	18.2	57.3	49.7	1.18
3. V-shaped	15.8	49.5	48.6	1.04
4. W-shaped	19.6	62.3	50.4	1.26
5. Scalloped	18.6	59.0	50.1	1.20
6. U-shaped	18.8	59.6	50.3	1.21
7. Undercut at trench bottom	18.6	59.4	50.2	1.21

Notations: S is the spectral sensitivity at $\lambda = 670$ nm; U_{br} is the breakdown voltage; M and M/U_{sup} are the unnormalized multiplication factor and that normalized to the supply voltage U_{sup}; $U_{sup} = 0.98U_{br}$.

In the third stage, we analyzed how narrowing of the profile at the trench bottom affects the multiplication factor. Fig. 5 shows the multiplication factor and spectral sensitivity versus the trench width, W_b, at the bottom. The dependences are well fitted by straight lines:

$$y = 2.9825x + 16.0922,\ R^2 = 0.9728 \text{ (for } S\text{)},$$

$$y = 10.3498x + 50.2300,\ R^2 = 0.9786 \text{ (for } M\text{)}.$$

The resulting dependences $M(W_b)$ and $S(W_b)$ can be rewritten as linear functions of the change in trench width:

$$M(W_b) = M(W_{b(\max)}) - x_1\Delta W_b,\ S(W_b) = S(W_{b(\max)}) - x_2\Delta W_b, \quad (4)$$

where $W_{b(\max)}$, μm, is the maximum width at the trench bottom (rectangular trench profile); ΔW_b, μm, is the deviation of the trench bottom width from its value for the rectangular profile; x_1 and x_2 are the linearization coefficients for M and S, respectively ($x_1 \approx 10$, $x_2 \approx 3$).

Fig. 6 shows the magnitude of the electric field strength and its lateral component versus the STI profile depth.

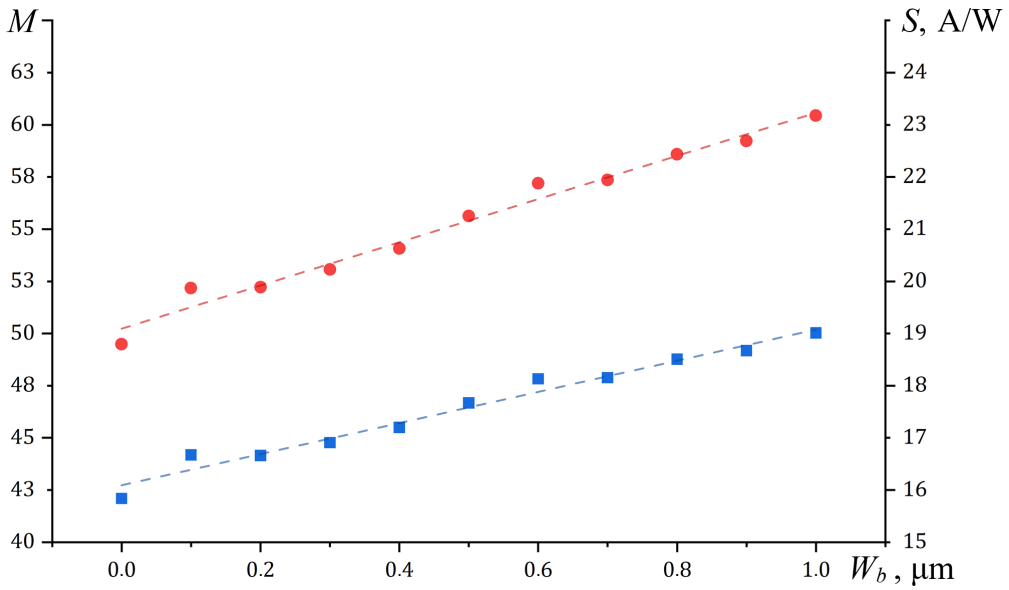


Fig. 5. Multiplication factor M (red symbols) and spectral sensitivity S (blue symbols) versus trench width W_b at the trench bottom. The fitting lines are shown as dashed lines

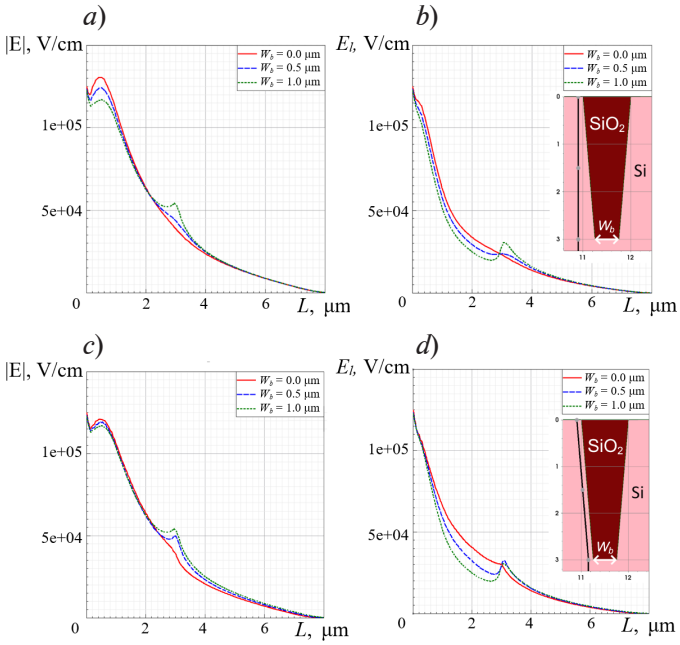


Fig. 6. Magnitude of electric field strength (*a*, *c*) and its lateral component (*b*, *d*) versus STI profile depth for three values of the bottom width W_b and different positions relative to the STI boundaries (the directions are indicated by black segments in the insets): 0.1 μm perpendicular to the upper STI boundary (*b*); along a line parallel to the lateral STI boundary with a 0.1 μm gap (L < 3 μm) and perpendicular to the surface (L > 3 μm) (*d*). U_{sup} = 40 V

The lateral field component along the chosen axis is stronger for the narrowed profile in the depth range below 3 μm, where the light intensity is highest. As a result, ionization processes in the lateral direction contribute more when the electric field reaches a critical value, which triggers premature breakdown of the avalanche photodiode.

Conclusion

We studied CMOS-compatible avalanche photodiode structures with shallow trench isolation (STI) as a guard ring. The following key parameter values were obtained at a supply voltage $U_{sup} = 0.98U_{br}$ ($\lambda = 670$ nm) by simulating the fabrication process and the output characteristics of the avalanche photodiode: a multiplication factor $M = 62.3$ and a spectral sensitivity $S = 19.6$ A/W.

The simulations for a SiO_2 trench width of about 1 μm showed that the optimal depth is about 3–4 μm, which rules out single-step isotropic silicon etching. The drop in M can reach 30% for etching with an aspect ratio of 1:1.

We found that defects causing the STI profile to narrow toward the trench bottom can reduce the multiplication factor M by up to 18%. Deviations of M from the optimum do not exceed 2.5% for the other defect types considered.

The dependences of the multiplication factor and spectral sensitivity on the profile width at the trench bottom are well approximated by linear functions expressed in terms of the deviation from the ideal profile. The decrease in the multiplication factor with the narrowing of the trench is associated with an increased contribution of the lateral component of the electric field in the region with the highest light intensity.

In the future, we plan to analyze the processes leading to a decrease in W_b, address the need to recalibrate the model, study the spectral dependences, and explore ways to minimize the effect of such technological defects and deviations on the multiplication factor of the avalanche photodiode.

REFERENCES

1. **Joo J. E., Lee M. J., Park S. M.,** A CMOS optoelectronic receiver IC with an on-chip avalanche photodiode for home-monitoring LiDAR sensors, Sensors, 21 (13) (2021) 4364.

2. **Wu Q.**, **Li Y., Yang Y., Chen S., Zhao Y.,**The law that guides the development of photolithography technology and the methodology in the design of photolithographic process, Proc. 2020 China Semiconductor Technology International Conference (CSTIC), Jun 26 –Jul 17, 2020, Shanghai, China, IEEE, (2020) 3–8.

3. **Furtado A. S., Diniz J. A., Monteiro D. W. D. L.,** Fabrication and characterization of active pixel sensors (APS) using simple metal gate nMOS technology, ECS Trans. 23 (1) (2009) 461.

4. **Goy J.**, **Courtois B., Karam J. M., Pressecq F.,** Design of an APS CMOS image sensor for low light level applications using standard CMOS technology, Analog Integr. Cir. Sig. Proc. 29 (1) (2001) 95–104.

5. **Kamrani E., Lesage F., Sawan M.,** Efficient premature edge breakdown prevention in SiAPD fabrication using the standard CMOS process, Semicond. Sci. Technol. 28 (4) (2013) 045008.

6. **Zhi W., Quan Q., Yu P., Jiang Y.,** A 45 nm CMOS avalanche photodiode with 8.4-GHz bandwidth, Micromachines. 11 (1) (2020) 65.

7. **Williams G. M., Huntington A. S.,** Probabilistic analysis of linear mode vs. Geiger mode APD FPAs for advanced LADAR enabled interceptors, In book: Howart R. T., Richards R. D. (Eds.) "Spaceborne Sensors III", Proc. SPIE. 6220 (30 May) (2006) 622008.

8. **Zhang Y., Wu Y., Sun Q., et al.,** Inductively coupled plasma dry etching of silicon deep trenches with extremely vertical smooth sidewalls used in micro-optical gyroscopes, Micromachines.14 (4) (2023) 846.

9. **Li L., Zhao X., Wong C. P.,** Charge transport in uniform metal-assisted chemical etching for 3D high-aspect-ratio micro-and nanofabrication on silicon, ECS J. Solid State Sci. Technol. 4 (9) (2015) P337–P346.

10. **Frühauf J., Krönert S.,** Wet etching of silicon gratings with triangular profiles, Microsyst. Technol.11 (12) (2005) 1287–1291.

11. **Hoekstra R. J., Kushner M. J., Sukharev V., Schoenborn P.,** Microtrenching resulting from specular reflection during chlorine etching of silicon, J. Vac. Sci. Technol. B. 16 (4) (1998) 2102–2104.

12. **Chang B., Leussink P., Jensen F.**, **et al.,** DREM: Infinite etch selectivity and optimized scallop size distribution with conventional photoresists in an adapted multiplexed Bosch DRIE process, Microelectron. Eng. 191 (5 May) (2018) 77–83.

13. **Panduranga P., Abdou A., Ren Zh., et al.,** Isotropic silicon etch characteristics in a purely inductively coupled SF6 plasma, J. Vac. Sci. Technol. B. 37 (6) (2019) 061206.

14. **Burtsev A., Li Y. X., Zeijl H. W., Beenakker C. I. M.,** An anisotropic U-shaped SF6-based plasma silicon trench etching investigation, Microelectron. Eng. 40 (2) (1998) 85–97.

15. **Laermer F., Urban A.,** Milestones in deep reactive ion etching, In book: Digest of technical papers of the 13th Int. Conf. on Solid-State Sensors, Actuators & Microsyst., Seoul, Korea (South), 05–09 June, 2005. TRANSDUCERS'05, IEEE, 2 (2005) 1118–1121.

16. **Hofbauer M., Schneider-Hornstein K., Zimmermann H.,** Single-photon detection for data communication and quantum systems, IOP Publishing, 2053–2563, Bristol (UK), 2021.

17. **Sze S. M., Yiming Li, Ng K. K.,** Physics of semiconductor devices, Second Ed., Wiley, New York, 1981.

18. **Van Overstraeten R., De Man H.,** Measurement of the ionization rates in diffused silicon *p–n* junctions, Solid State Electron.13 (5) (1970) 583–608.

19. **Chynoweth A. G.,** Chynoweth, ionization rates for electrons and holes in silicon, Phys. Rev. 109 (5) (1958) 1537–1540.

20. **Lee M. J., Choi W. Y.,** Performance optimization and improvement of silicon avalanche photodetectors in standard CMOS technology, IEEE J. Sel. Top. Quantum Electron. P-P (20 Sept) (2017) 1–1.

21. **Wang W., Zeng H.-A., Wang F., et al.,** A speed-optimized, low-noise APD with 0.18 μm CMOS technology for the VLC applications, Mod. Phys. Lett. B, 34 (29) (2020) 2050321.

СПИСОК ЛИТЕРАТУРЫ

1. **Joo J. E., Lee M. J., Park S. M.** A CMOS optoelectronic receiver IC with an on-chip avalanche photodiode for home-monitoring LiDAR sensors // Sensors. 2021. Vol. 21. No. 13. P. 4364.

2. **Wu Q.**, **Li Y., Yang Y., Chen S., Zhao Y.** The law that guides the development of photolithography technology and the methodology in the design of photolithographic process // Proceedings of the 2020 China Semiconductor Technology International Conference (CSTIC). June 26 –July 17, 2020, Shanghai, China, IEEE, 2020. Pp. 3–8.

3. **Furtado A. S., Diniz J. A., Monteiro D. W. D. L.** Fabrication and characterization of active pixel sensors (APS) using simple metal gate nMOS technology // ECS Transactions. 2009. Vol. 23. No. 1. P. 461.

4. **Goy J.**, **Courtois B., Karam J. M., Pressecq F.** Design of an APS CMOS image sensor for low light level applications using standard CMOS technology // Analog Integrated Circuits and Signal Processing. 2001. Vol. 29. No. 1–2. Pp. 95–104.

5. **Kamrani E., Lesage F., Sawan M.** Efficient premature edge breakdown prevention in SiAPD fabrication using the standard CMOS process // Semiconductor Science and Technology. 2013. Vol. 28. No. 4. P. 045008.

6. **Zhi W., Quan Q., Yu P., Jiang Y.** A 45 nm CMOS avalanche photodiode with 8.4-GHz bandwidth // Micromachines. 2020. Vol. 11. No. 1. P. 65.

7. **Williams G. M., Huntington A. S.** Probabilistic analysis of linear mode vs. Geiger mode APD FPAs for advanced LADAR enabled interceptors // Howart R. T., Richards R. D. (Eds.). Spaceborne Sensors III. Proceedings SPIE. 2006. Vol. 6220. 30 May. P. 622008.

8. **Zhang Y., Wu Y., Sun Q., Shen L., Lan J., Guo L., Shen Zh., Wang X., Xiao J., Xu J.** Inductively coupled plasma dry etching of silicon deep trenches with extremely vertical smooth sidewalls used in micro-optical gyroscopes // Micromachines. 2023. Vol. 14. No. 4. P. 846.

9. **Li L., Zhao X., Wong C.-P.** Charge transport in uniform metal-assisted chemical etching for 3D high-aspect-ratio micro-and nanofabrication on silicon // ECS Journal of Solid State Science and Technology. 2015. Vol. 4. No. 9. Pp. P337–P346.

10. **Frühauf J., Krönert S.** Wet etching of silicon gratings with triangular profiles // Microsystem Technologies. 2005. Vol. 11. No. 12. Pp. 1287–1291.

11. **Hoekstra R. J., Kushner M. J., Sukharev V., Schoenborn P.** Microtrenching resulting from specular reflection during chlorine etching of silicon // Journal of Vacuum Science & Technology B: Microelectronics and Nanometer Structures Processing, Measurement, and Phenomena. 1998. Vol. 16. No. 4. Pp. 2102–2104.

12. **Chang B., Leussink P., Jensen F., Hübner J., Jansen H.** DREM: Infinite etch selectivity and optimized scallop size distribution with conventional photoresists in an adapted multiplexed Bosch DRIE process // Microelectronic Engineering. 2018. Vol. 191. 5 May. Pp. 77–83.

13. **Panduranga P., Abdou A., Ren Zh., Pedersen R. H., Nezhad M. P.** Isotropic silicon etch characteristics in a purely inductively coupled SF6 plasma // Journal of Vacuum Science & Technology B. 2019. Vol. 37. No. 6. P. 061206.

14. **Burtsev A., Li Y. X., Zeijl H. W., Beenakker C. I. M.** An anisotropic U-shaped SF6-based plasma silicon trench etching investigation // Microelectronic Engineering. 1998. Vol. 40. No. 2. Pp. 85–97.

15. **Laermer F., Urban A.,** Milestones in deep reactive ion etching // Digest of technical papers (Vol. 2) of the 13th International Conference on Solid-State Sensors, Actuators and Microsystems (TRANSDUCERS'05), Seoul, Korea (South), 05–09 June, 2005. IEEE. 2005, Pp. 1118–1121.

16. **Hofbauer M., Schneider-Hornstein K., Zimmermann H.**, Single-photon detection for data communication and quantum systems. Bristol (UK): IOP Publishing, 2053–2563, 2021.

17. **Зи С.** Физика полупроводниковых приборов. Пер. с англ. М.: Рипол Классик, 1973. 655 с.

18. **Van Overstraeten R., De Man H.** Measurement of the ionization rates in diffused silicon *p–n* junctions // Solid State Electronics. 1970. Vol. 13. No. 5. Pp. 583–608.

19. **Chynoweth A. G.** Ionization rates for electrons and holes in silicon // Physical Review. 1958. Vol. 109. No. 5. Pp. 1537–1540.

20. **Lee M.-J., Choi W.-Y.** Performance optimization and improvement of silicon avalanche photodetectors in standard CMOS technology// IEEE Journal of Selected Topics in Quantum Electronics. 2017. Vol. P-P. 20 September. Pp. 1–1.

21. **Wang W., Zeng H.-A., Wang F., Wang G., Xie Y., Feng Sh.** A speed-optimized, low-noise APD with 0.18 μm CMOS technology for the VLC applications // Modern Physics Letters B. 2020. Vol. 34. No. 29. P. 2050321.

THE AUTHORS

DOLZHENKO Dmitry I.
Peter the Great St. Petersburg Polytechnic University
29 Politechnicheskaya St., St. Petersburg, 195251, Russia
ddi.dev.94@gmail.com
ORCID: 0000-0002-5707-4145

LETKIMAN Egor D.
Peter the Great St. Petersburg Polytechnic University
29 Politechnicheskaya St., St. Petersburg, 195251, Russia
letkiman.egor@gmail.com

СВЕДЕНИЯ ОБ АВТОРАХ

ДОЛЖЕНКО Дмитрий Игоревич – *кандидат физико-математических наук, старший преподаватель Высшей школы электроники и микросистемной техники Санкт-Петербургского политехнического университета Петра Великого.*
195251, Россия, г. Санкт-Петербург, Политехническая ул., 29
ddi.dev.94@gmail.com
ORCID: 0000-0002-5707-4145

ЛЕТКИМАН Егор Дмитриевич – *студент Института электроники и телекоммуникаций Санкт-Петербургского политехнического университета Петра Великого.*
195251, Россия, г. Санкт-Петербург, Политехническая ул., 29
letkiman.egor@gmail.com

Received 11.12.2025. Approved after reviewing 26.12.2025. Accepted 02.02.2026.
Статья поступила в редакцию 11.12.2025. Одобрена после рецензирования 26.12.2025. Принята 02.02.2026.

© Peter the Great St. Petersburg Polytechnic University, 2026